Correspondence between dynamic higher-order topological insulator and synthetic higher-order Dirac semimetal

Haonan Wang[1], Hui Liu[1],[*] Yuanshuo Liu[1], Yugan Tang[1], Pengtao Lai[1], Hua Cheng[1],[†] and Shuqi Chen[1,2,3][‡]

[1] *The Key Laboratory of Weak Light Nonlinear Photonics, Ministry of Education, School of Physics and TEDA Institute of Applied Physics, Nankai University, Tianjin 300071, China*

[2] *School of Materials Science and Engineering, Smart Sensing Interdisciplinary Science Center, Nankai University, Tianjin 300350, China and*

[3] *The Collaborative Innovation Center of Extreme Optics, Shanxi University, Taiyuan, Shanxi 030006, China*

(Dated: April 27, 2025)

S-I TIGHT-BINDING HAMILTONIAN

The tight-binding Hamiltonian $H(k_x, k_y, \phi)$ is invariant under time-reversal symmetry, inversion symmetry and C_6 rotation symmetry along the ϕ axis, which support a pair of Dirac points located along the rotation axis. There are two doubly degenerate states p_x/p_y, $d_{x,y}/d_{x^2-y^2}$ along ΓA protected by C_{3v} symmetry which has a 2D irreducible representation, as shown in Fig. 1(c). The tight-binding Hamiltonian $H(k_x, k_y, \phi)|_{k_x=k_y=0}$ along the rotation axis in the basis $(p_x, p_y, d_{x,y}, d_{x^2-y^2})^T$ is

$$H(\phi) = \begin{pmatrix} 2\delta\cos(\phi) & 0 \\ 0 & -2\delta\cos(\phi) \end{pmatrix} \otimes I_{2\times 2}, \tag{S1}$$

where $p_x = (1, 0, -1, -1, 0, 1)^T/2$, $p_y = (-1/2, -1, -1/2, 1/2, 1, 1/2)^T/\sqrt{3}$, $d_{x,y} = (-1, 0, 1, -1, 0, 1)^T/2$, $d_{x^2-y^2} = (-1/2, 1, -1/2, -1/2, 1, -1/2)^T/\sqrt{3}$. Along the ϕ axis, a pair of fourfold linear crossing points exist at $(0, 0, \pm 0.5\pi)$. The doubly degenerate dipolar and quadrupolar states can be hybridized as $p_\pm = p_x \pm ip_y$, $d_\pm = d_{x,y} \pm id_{x^2-y^2}$ with pseudospin up and pseudospin down. Based on $k \cdot p$ perturbation theory, the effective Hamiltonian near ΓA can be obtained by the hybridized states. The $H_{eff}(k_x, k_y, \phi)$ in the basis $(p_x + ip_y, d_{x,y} + id_{x^2-y^2}, p_x - ip_y, d_{x,y} - id_{x^2-y^2})^T$ can be written in the block-diagonal form

$$H_{eff}(k_x, k_y, \phi) = \begin{pmatrix} h(k_x, k_y, \phi) & 0 \\ 0 & h^*(-k_x, -k_y, -\phi) \end{pmatrix}, \tag{S2}$$

where $h(k_x, k_y, \phi) = \begin{pmatrix} 2\delta\cos(\phi) & A(k_x - ik_y) \\ A^*(k_x + ik_y) & -2\delta\cos(\phi) \end{pmatrix}$ and $A = (i + \sqrt{3})(t_0 - \delta\cos(\phi))/4$. The tight-binding Hamiltonian $H(k_x, k_y, \phi)$ expended with the hybridized states has a form similar to the minimal 4×4 Hamiltonian of a Dirac semimetal [1]. Thus, the pair of fourfold linear crossing points at $(0, 0, \pm 0.5\pi)$ are Dirac points which are created by a band inversion and located along the rotation axis ϕ.

S-II TOPOLOGICAL CHARGE OF THE DEGENERACY

The topological charge of these degenerate points can be captured by the evolution of Berry phase around the degenerate points [2, 3]. A small sphere, as closed integral region, parametrized by polar angle θ and azimuth angle φ, encloses the Dirac point in the Brillouin

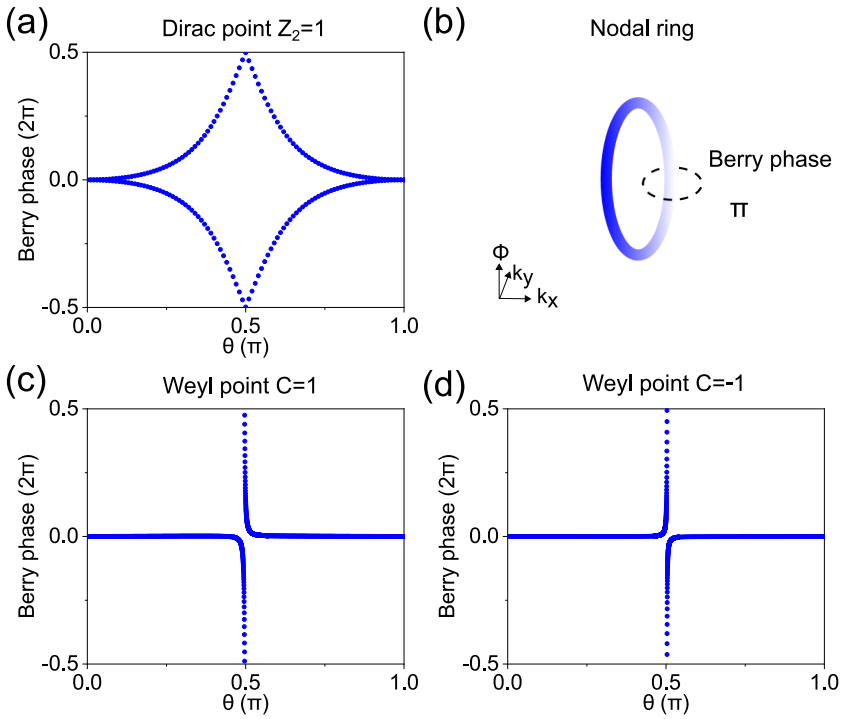

FIG. S1. The topological charge of Dirac point, nodal ring, and Weyl points. (a) The evolution of Berry phase over a sphere enclosing a Dirac point. (b) The Berry phase of π around a nodal ring. The evolution of Berry phase over spheres enclosing Weyl points with (c) $C = 1$ and (d) $C = -1$.

region. The evolution of Berry phase shows a gapless spectrum in Fig. S1(a), which indicates the Dirac point hosts a nonzero topological charge of $Z_2 = 1$. The nodal rings evolved from Dirac points has topologically nontrivial charge, which is revealed by the Berry phase of a closed loop threading a nodal ring, as illustrated in Fig. S1(b). For Weyl points, the Berry phase, around the twofold linear degeneracy at green and red spheres denoted in Fig. 1(f), shifts downwards in Fig. S1(c) but upwards in Fig. S1(d), corresponding to the Weyl points with topological charges of $C = 1$ and $C = -1$, respectively.

S-III CORNER STATES AT ACUTE AND OBTUSE-ANGLED CORNERS

Although topological corner states in the higher-order topologically nontrivial phase are protected by the bulk topological properties, the emergences of the topological states are crucially determined by the boundary conditions. Different shaped models can lead to different hopping conditions and reduce the symmetries of the lattice at the edges and corners. The existence of the chiral-symmetry-protected "zero-energy" corner states can be

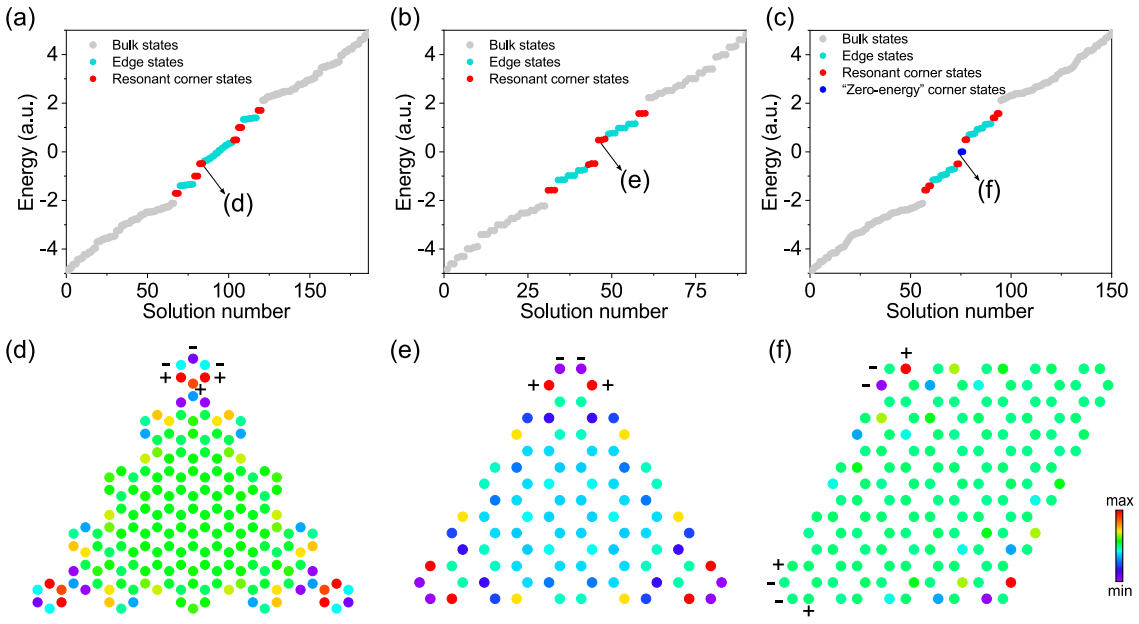

FIG. S2. Calculated energy spectrum for different shaped models. (a-c) Calculated energy spectrum for the triangle-shaped model with armchair boundary, triangle-shaped model with zigzag boundary, and parallelogram-shaped model, respectively. (d-f) Energy field distributions of the resonant corner states in (a, b), and "zero-energy" corner state in (c), respectively. The + and – represent chiral charge of +1 and -1 respectively.

characterized by a topological index $N = |N_+ - N_-|$ which captures the interplay between the bulk topological properties and boundary conditions [4, 5]. $N_\pm$ are the number of eigenstates with chiral topological charge ± 1 at the lattice points. Based on the tight-binding Hamiltonian model, we calculated energy spectrum of the finite-size model with different shapes at $\phi = 0$ in higher-order topological phase. The calculated energy spectrum of two-type triangle-shaped models fail to identify "zero-energy" corner states as shown in Figs. S2(a) and S2(b). But the resonant corner states can be found in the energy spectrum denoted by red dots, with energy field distributions shown in Figs. S2(d) and S2(e). The two-type triangle-shaped models have $N = |3 - 3| = 0$ and $N = |2 - 2| = 0$ at the corners indicates that there are no "zero-energy" corner states. Figure S2(c) shows the calculated energy spectrum of the parallelogram-shaped model with zigzag boundary and it is obvious to see the "zero-energy" corner states denoted by blue dots. The "zero-energy" corner states only exist at the $2\pi/3$ corners which have $N = |1 - 2| = 1$, as depicted in Fig. S2(f). The topological index $N = |2 - 2| = 0$ at the $\pi/3$ corners implies that there are no "zero-energy"

corner states. Thus, the topologically protected "zero-energy" corner states can arise at the $2\pi/3$ corners with $N = 1$ but not the $\pi/3$ corners with $N = 0$.

S-IV DIFFERENT HIGHER-ORDER TOPOLOGICAL PHASES TRANSFORMED FROM HODSM

How HODSM in 3D synthetic space evolves into different higher-order topological phases such as HONRSM, HOWSM, and 3D HOTI by breaking the symmetry or accurately adjusting the coupling strength is analyzed in detail here. The C_{6v} symmetry is broken into C_{2v} symmetry by adding nonzero on-site potential at the 1 and 4 sites with $e_1 = e_4 = -0.8$ as shown in Fig. S3(a), and each Dirac point will split into a nodal ring. The bulk band structures for the nodal ring evolved from a Dirac point is plotted in Fig. S3(b). The corresponding high-order topological invariant is shown in Fig. S3(c), which is topologically nontrivial ($[M_1^{(2)}] = -2$) between two nodal rings. For a finite-size hexagonal model, the projected energy band exists topological hinge states denoted by blue dots in Fig. S3(d), arising from higher-order nontrivial topological phase. The topological invariant $[M_1^{(2)}]$ is not well defined in the gapless nodal-ring region. The topological hinge states are no longer located at zero energy because of the violation of chiral symmetry caused by nonzero on-site potential.

Further introducing complex couplings into the intracell couplings as $t_1(\phi) = t_0 + \delta e^{i\phi}$ to generate synthetic gauge flux, nodal ring degeneracy will be split into Weyl degeneracy. The black arrows represent the direction of positive phase hopping, as shown in Fig. S3(e). A nodal ring degeneracy evolves into a pair of Weyl points with opposite topological charges denoted by green and red spheres, as illustrated in Fig. S3(f). The topological invariant $[M_1^{(2)}] = -2$ and $[M_1^{(2)}] = -1$ exhibit a hybrid topological phase, which combines second-order and first-order topological phase, as shown in Fig. S3(g). Topological hinge states denoted by blue dots appear in the second-order phase as shown in Fig. S3(h). In the first-order topological phase, surface states denoted by green dots are embedded in the bulk states between the pair of Weyl points evolved from the same Dirac point.

Without breaking C_{6v} symmetry, the HODSM can transition to a 3D HOTI by simply adjusting the coupling strength, as shown in Fig. S3(i). When intra- and intercell couplings are accurately modulated as $t_1(\phi) < t_2(\phi)$ over the entire period, such as $t_1(\phi) = -1 +$

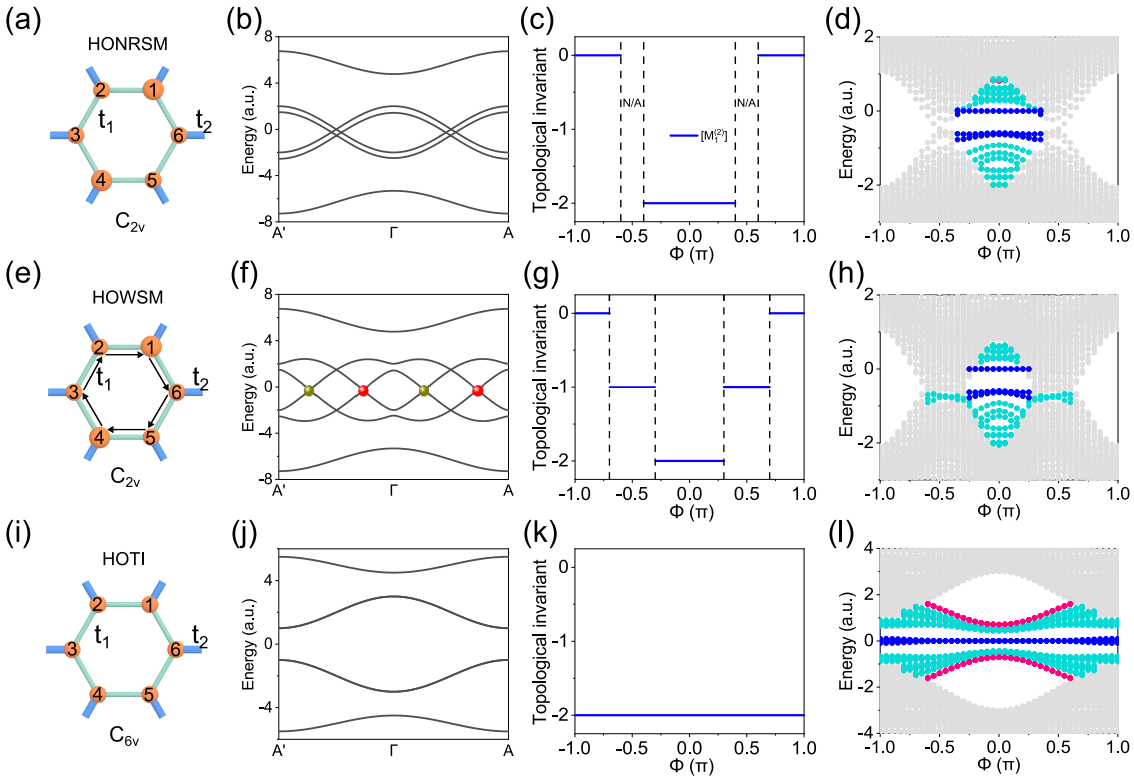

FIG. S3. HONRSM, HOWSM, and 3D HOTI transformed from HODSM. (a, e, i) Unit cell of tight-binding model, (b, f, j) bulk band structures along ΓA, (c, g, k) topological invariant $[M_1^{(2)}]$ along ϕ direction, and (d, h, l) projected band dispersions for HONRSM, HOWSM, and 3D HOTI, respectively. Gray. red, green, and blue dots indicate bulk, surface, trivial hinge, and topological hinge states, respectively.

$0.5\cos(\phi)$ and $t_2(\phi) = -3 - 0.5\cos(\phi)$, the dynamic 2D system keeps a 2D HOTI for all ϕ. The band gap is opened along ΓA, as shown in Fig. S3(j). The topological invariant is $[M_1^{(2)}] = -2$ for all ϕ in Fig. S3(k), which results in the topological hinge states denoted by blue dots in the topologically nontrivial gap, as shown in Fig. S3(l).

S-V ROBUSTNESS OF THE HIGHER-ORDER HINGE STATES

To investigate the robustness of "zero-energy" higher-order hinge states, we introduce disorder into different regions of the hexagonal acoustic crystal and calculate the corresponding eigenfrequencies. First, we consider a finite-size hexagonal acoustic crystal with disorder in both bulk and edge sites, denoted by gray dots in Fig. S4(a). Then, we introduce disorder

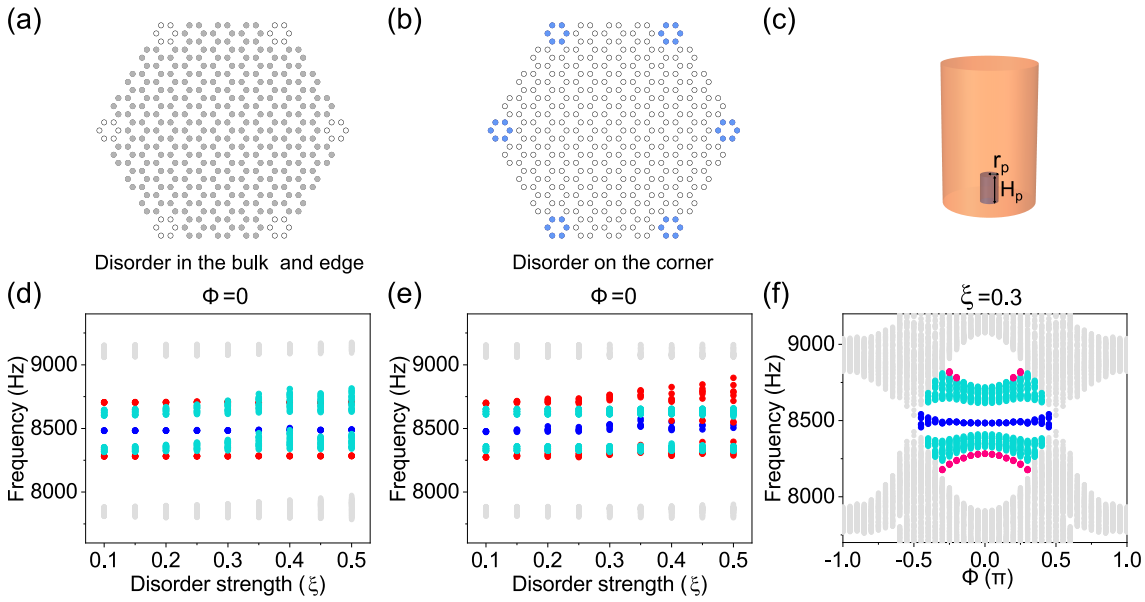

FIG. S4. Robustness of the higher-order hinge states. The finite-size hexagonal acoustic crystal with (a) disorder in bulk and edge sites denoted by gray dots and (b) disorder on the corner sites denoted by blue dots. (c) Illustration of the disorder introduced in an acoustic cavity. Simulated eigenfrequencies of the hexagonal acoustic crystal with (d) disorder in the edge and bulk sites, and (e) disorder only on the corner sites, as a function of different disorder strength ξ. (f) For disorder strength $\xi = 0.3$, simulated projected band dispersions of the hexagonal acoustic crystal with disorder in the edge and bulk sites.

only to the corner sites denoted by blue dots in Fig. S4(b). Here, disorder is introduced by adding a "hard" perturbation cylinder with radius r_p and height $H_p = 0.2H$ at the bottom of the acoustic cavity, as shown in Fig. S4(c). The radius r_p is a random number randomly spread in $(0,\ \xi r_0)$ detuned by the disorder strength ξ. When disorder is introduced in the bulk and edge sites, the eigenfrequencies of the hexagonal acoustic crystal at $\phi = 0$ show that the topological corner states (blue dots) are stable against the disorder, as shown in Fig. S4(d). The trivial corner states (red dots) submerge into the edge states (green dots) in large disorder strength. When disorder is only introduced on the corner sites, both corner states show a little shift towards higher frequencies, as shown in Fig. S4(e). The topologically protected corner states are more robust than the trivial corner states. For $\xi = 0.3$, the simulated projected band dispersions of the hexagonal acoustic crystal with disorder in the bulk and edge sites are potted in Fig. S4(f), which illustrate that the higher-order hinge

states (blue dots) constituted by topological corner states, are almost unaffected by small disorder and more robust than the trivial ones (red dots).

S-VI EXPERIMENTAL MEASUREMENTS, LDOS, AND NUMERICAL SIMULATIONS

1. Experimental measurements and LDOS

The samples were fabricated by 3D printing with UV resin. The intra- and intercell couplings of each sample are modulated by parameter ϕ. Each sample contains 366 resonators and one of the samples with $\phi = 0$ is shown in Fig. 3(a). A balanced armature speaker (Knowles WBFK30095) and a 1/8-inch diameter microphone (B&K Type 2670) were placed at the bottom and top of the same resonator to probe the local pressure response. The pressure responses $\mathrm{X}(\omega, \phi)$ at each frequency were obtained by the Fourier transformations performed in the network analyzer (Keysight E5061B). Probing the resonators one by one, we got the acoustic pressure field distribution $\mathrm{X}(i, \omega, \phi)$ for each site i. The LDOS of the corner states can be calculated as follows [6]: First, we normalized the pressure responses on the total spectra summed over frequencies and the free-space pressure response in air, $\mathrm{X}(i, \omega, \phi) = \chi(i, \omega, \phi) / \sum_\omega \chi(i, \omega, \phi) / \chi_{air}(\omega)$. Second, we squared the $\mathrm{X}(i, \omega, \phi)$ and averaged the power spectrum for the higher-order corner states localized at A and B resonators, $P_a(\omega, \phi) = \sum_{i \in A,B} |\mathrm{X}(i, \omega, \phi)|^2 / N_{AB}$, $N_{AB} = 12$. Finally, we normalized the power spectra to get the LDOS of the corner states, $P_n(\omega, \phi) = P_a(\omega, \phi) / \sum_{i \in \omega} P_a(\omega, \phi)$. The measured acoustic pressure fields at 8485 Hz in Fig. 3(d) were obtained by measuring the local pressure response at each site for different values ϕ.

2. Numerical simulations

All the simulated results were performed by COMSOL Multiphysics based on the finite-element method. The boundaries of acoustic crystals were viewed as acoustically rigid due to the huge impedance mismatch between UV resin and air. The sound speed was set as $344\ \mathrm{m \cdot s^{-1}}$ and the density of air was set as $1.2\ \mathrm{kg \cdot m^{-3}}$. To simulate the bulk band structures, periodic boundary conditions were applied along the x and y directions of the

unit cell. A hexagonal structure with a side length $L = 5a$ was used to simulate the projected band dispersions along the parameter ϕ. The acoustic eigenpressure fields in Fig. 2(d) were calculated by the eigenvalue solver using the pressure acoustics module. Through full-wave simulation, we obtained the local pressure response spectra to get the simulated LDOS and the excited acoustic pressure fields. To better match the real situation, the speed of sound was set as $344(1 + 0.005i)$ m $\cdot$ s^{-1} in full-wave simulation, where the small imaginary part mimics the loss of sound.

* Corresponding author: hliu@nankai.edu.cn

† Corresponding author: hcheng@nankai.edu.cn

‡ Corresponding author: schen@nankai.edu.cn

[1] B.-J. Yang and N. Nagaosa, Classification of stable three-dimensional dirac semimetals with nontrivial topology, Nature communications **5**, 4898 (2014).

[2] R. Yu, X. L. Qi, A. Bernevig, Z. Fang, and X. Dai, Equivalent expression of z2 topological invariant for band insulators using the non-abelian berry connection, Physical Review B **84**, 075119 (2011).

[3] B. Xie, H. Liu, H. Cheng, Z. Liu, J. Tian, and S. Chen, Dirac points and the transition towards weyl points in three-dimensional sonic crystals, Light: Science & Applications **9**, 201 (2020).

[4] J. Noh, W. A. Benalcazar, S. Huang, M. J. Collins, K. P. Chen, T. L. Hughes, and M. C. Rechtsman, Topological protection of photonic mid-gap defect modes, Nature Photonics **12**, 408 (2018).

[5] J. C. Teo and C. L. Kane, Topological defects and gapless modes in insulators and superconductors, Physical Review B **82**, 115120 (2010).

[6] X. Ni, M. Weiner, A. Alu, and A. B. Khanikaev, Observation of higher-order topological acoustic states protected by generalized chiral symmetry, Nature materials **18**, 113 (2019).